Experimental Thermal and Fluid Science 60 (2015) 54–65

Contents lists available at ScienceDirect

Experimental Thermal and Fluid Science

journal homepage: www.elsevier.com/locate/etfs

Computer-controlled Two-Roll Mill flow cell for the experimental study of particle and drop dynamics

Israel Y. Rosas [a,*], Marco A.H. Reyes [b], A.A. Minzoni [c], E. Geffroy [a]

[a] Instituto de Investigaciones en Materiales, Universidad Nacional Autónoma de México, Apdo. Postal 70-360, Circuito Exterior, Cd. Universitaria, Coyoacán, 04510 México, DF, Mexico
[b] Departamento de Termofluidos, Facultad de Ingeniería, Universidad Nacional Autónoma de México, Circuito Exterior, Cd. Universitaria, Coyoacán, 04510 México, DF, Mexico
[c] FENOMEC, Instituto de Investigaciones en Matemáticas Aplicadas y Sistemas, Universidad Nacional Autónoma de México, Apdo. Postal 20-726, Circuito Exterior, Cd. Universitaria, Coyoacán, 04510 México, DF, Mexico

ARTICLE INFO

Article history:
Received 3 May 2013
Received in revised form 11 August 2014
Accepted 12 August 2014
Available online 23 August 2014

Keywords:
Two-Roll Mill
Flow-type parameter
Nonlinear control
Drop deformation

ABSTRACT

In this paper, we present for the deformation of a drop under flow, using an experimental device based on the Two-Roll Mill geometry. To study the drop deformation for extended periods of time, the use of this device requires implementation of a non-linear control scheme that has not previously been used. The device and control scheme generate well characterized flow fields, which present a richness of behavior of the drop dynamics that smoothly varies from that observed in simple shear flows, where the vorticity dominates, to those observed in purely Hyperbolic flows. The Two-Roll Mill flow cell allows detailed studies such as the critical capillary number versus the critical viscosities ratio for elongational flows with significant vorticity. As well, the experimental device is able to track the time evolution of the drop shape permitting to study its complex time evolutions. Experiments were performed for sub-millimeter size drops with the determination of the surface tension with high accuracy.

1. Introduction

The deformation and break-up of a single drop within a stress field are phenomena of great relevance in countless important industrial operations. Also, the drop dynamics can be extrapolated to a qualitative understanding of more concentrated systems, such as those in the food and pharmaceutical emulsions, paint manufacturing and polymer processes among others, see for example references in [1–12]. Many researchers have contributed to this knowledge, beginning with the pioneering work of Taylor [13] which includes both theoretical analysis and experimental observations, focused on the deformation of single drops suspended in a second liquid. In general, Taylor's work showed that when a drop with radius r_0 and viscosity μ_0 is immersed in a second immiscible fluid with viscosity μ_1, and is subjected to a shear-rate $\dot{\gamma}$ in a flow field, the deformation will depend basically on: (1) the viscosity ratio between the drop and the continuous phase, $\lambda = \mu_0/\mu_1$; (2) the capillary number defined as $Ca = r_0\mu_1\dot{\gamma}/\sigma$, which relates the magnitude of the viscous stresses acting to deform the drop and the magnitude of the stresses due to the interfacial tension σ on the interface, that opposes to the drop deformation; and (3) the flow field applied, where the deformation rates and its vorticity are the two most important parameters.

Most theoretical and experimental studies on drop deformation—under flows not driven by pressure differentials—have addressed the fluid dynamics effects using two types of flow fields: simple shear flows (where the magnitudes of the vorticity and the strain rate are equal) and pure extensional flows (with no vorticity). The two most frequently used experimental devices used to generate these flows were: the Parallel Band apparatus **PB** (for simple shear) and the Four-Roll Mills apparatus **FRM** (for planar elongation). Major experimental contributions to our understanding of the dynamics of a drop in simple shear flow are due to Rumscheidt and Mason [14], Torza et al. [15], Grace [16] and more recently by Guido and Villone [17], Guido et al. [18,19], Guido and Greco [20], Birkhofer et al. [21] and Megias-Alguacil et al. [1]. These include measurements of the critical capillary number for break-up of drop in simple shear flows, [16], and computer controlled versions of the shear band apparatus [17,21].

An exception to the use of simple shear flows are studies using four-cylinder flow devices, which allow a richer set of flow fields and are capable of inducing large deformation of a drop, hence its usefulness to study its nonlinear dynamics. In 1934, Taylor [13] used these, with a manual control, subjecting a drop to an elongational flow for an extended period. Much later, Leals groups at Caltech and UCSB—see for example: Bentley and Leal [22,23],

* Corresponding author. Tel.: +52 55 5622 4630.
E-mail address: isroye@yahoo.com.mx (I.Y. Rosas).

http://dx.doi.org/10.1016/j.expthermflusci.2014.08.006
0894-1777/

Nomenclature

B	shortest axes of the ellipsoidal drop cross-section (m)
Ca	capillary number, $Ca = r_0\mu_1\dot{\gamma}/\sigma$
Ca_{crit}	critical capillary number
D	deformation parameter used for the interfacial tension calculus $D = \Lambda_1 - \Lambda_2$
D_0	initial deformation in the retraction process, measured with Taylor deformation D_T
D_T	Taylor deformation parameter (L – B)/(L + B)
de	distance that separates the axes of the rotating cylinders (m)
$\boldsymbol{E}$	rate of deformation tensor $\boldsymbol{E} = (\nabla u + \nabla u^T)/2$
$\mathrm{II}_{2\boldsymbol{E}}$	second invariant of $\boldsymbol{E}$
L	longest axes of the ellipsoidal drop cross-section (m)
R	radius of the cylinders (m)
r_0	drop initial radius (m)
$\boldsymbol{S}$	second rank tensor used by Maffetone [47] to describe the drop shape
$\bar{\boldsymbol{w}}$	vorticity tensor, Astarita [26]
$\nabla\boldsymbol{u}$	velocity gradient tensor

Greek symbols

α	flow type parameter $\alpha = \frac{\|\boldsymbol{E}\| - \|\bar{\boldsymbol{w}}\|}{\|\boldsymbol{E}\| + \|\bar{\boldsymbol{w}}\|}$
$\dot{\gamma}$	shear rate $\dot{\gamma} = \sqrt[2]{\|\mathrm{II}_{2\boldsymbol{E}}\|}$ (1/s)
θ	orientation angle of the longest axes L respect to the x-axis (degrees°)
Λ	eigenvalues of the tensor $\boldsymbol{S}$
λ	viscosity ratio $\lambda = \mu_0/\mu_1$
μ	dynamic viscosity (Pa s)
σ	interfacial tension (N/m)
ϕ	half the angle between the incoming and outgoing axes (degrees °)
ω	angular velocity of the cylinders (rad/s)

Stone et al. [24], Milliken et al. [25]—used a precise computer-based control for the FRM to study the deformation of a drop under flow conditions, other than pure extensional, for extended periods of time, while applying complex flow histories. These flow fields cover a wide range of planar elongational—Hyperbolic—flows that, on one end, asymptotically approach a simple shear flow condition, and at the other, a purely 2*D*-extensional flow.

This family of 2-dimensional flows can be characterized by the *flow-type parameter* α that prescribes the velocity gradient tensor $\nabla\boldsymbol{u}$ of the flow field at the region centered within the 4 cylinders, and specifies the ratio of the magnitude of the rate of deformation tensor to that of the vorticity

$$\frac{\text{magnitude of deformation rate}}{\text{magnitude of vorticity}} = \frac{1+\alpha}{1-\alpha}. \tag{1}$$

Thus, α is given by

$$\alpha = \frac{\|\boldsymbol{E}\| - \|\bar{\boldsymbol{w}}\|}{\|\boldsymbol{E}\| + \|\bar{\boldsymbol{w}}\|}, \tag{2}$$

where $\boldsymbol{E} = (\nabla\boldsymbol{u} + \nabla\boldsymbol{u}^T)/2$ is the rate of deformation tensor. The vorticity tensor $\bar{\boldsymbol{w}}$ [26], measures the rate of rotation of a material point with respect to the rate of deformation's principal axes at that point. The case of $\alpha = -1$ corresponds to a pure rotational flow, $\alpha = 0$ to simple shear flow, and $\alpha = 1$ describes a pure extensional flow. Flows with α values between $-1 < \alpha \leqslant 0$ are classified as *weak*, because they have significant amounts of vorticity and are not expected to produce large deformations on an embedded object. On the contrary, flow fields with α values between $0 < \alpha \leqslant 1$ induce significant deformations because two neighboring elements of fluids separate in time exponentially, so the flow induces significant changes on the microstructure of the fluid; these are classified as *strong flows* [27,28].

The central region of the FRM flow has a stagnation point; thus, it is possible to study a deformed drop under well characterized extensional flows and for long periods of time. However, maintaining the position of the drop is quite difficult as the velocity field about the stagnation point is an unstable saddle point; i.e., carrying out these experiments manually is possible only for a short time. During the 1980s, Bentley and Leal [22,23] perform a series of experimental studies for strong flows with α values different from zero or one, using a computer-controlled version of Taylor's setup, coupled with modern camera technology. The setup objective was to cancel the permanent drift of the drop away from the stagnation point due to its saddle-point condition. Real-time video monitoring of the drop position allows implementation of a feedback loop, where the stagnation point location is adjusted for minimum drift while the flow-field deformation parameters remain steady. The control scheme adjusts individually the rotational speed of all cylinders—4 degrees of freedom—and displaces the instantaneous position of the stagnation point within a small region of the flow. The stagnation point is proportionally relocated towards the drop centroid position in the flow to cancel the drift of the drop. By maintaining the drop within this region, its residence time can be very long given that the drift field is negligible.

However, for small α values (say, less than 0.3), one pair of cylinders is rotating significantly slower than the other. For these cases, the performance of the linear control-scheme deteriorates. Studies by Bentley and Leal [22], and Yang et al. [29], using the FRM device, show that the most effective range of α values are within $0.4 \leqslant \alpha \leqslant 1$. So, even while four-roll mills and parallel band devices cover a wide interval of the flow-type parameter values appropriate for drop dynamics, there is still a gap in flow type studies in which a strong competition of vorticity and deformation dynamics may affect the time evolution of highly deformed drops. Besides, on one hand, the qualitative behavior for deformation of drops in flows with $0.6 \leqslant \alpha$ is very similar to that for $\alpha = 0.2$, see Fig. 28 in Ref. [23]; on the other, the drop behavior for flow types with values of $\alpha = 0$ differs greatly from those with values of α higher than 0.2.

In order to fill this gap of knowledge and cover a range of flow parameters not previously studied, the co-rotating Two-Roll Mill can be used. This device is particularly effective for flows covering the remaining gap in α values; i.e., between $0.03 \leqslant \alpha \leqslant 0.3$ [30–32]. But this proposition comes with a caveat: the lack of a linear control algorithm to maintain the drop at the stagnation point in a two-dimensional flow field. In essence, a control scheme based on the intrinsic hydrodynamics of the Two-Roll Mill is needed, while allowing for robust closed trajectories of the drop about the stagnation point.

With this flow geometry, the modification of the rotational speed of the cylinders displaces the stagnation point position along a direction transversal to the drift of the drop centroid. Hence, there is no possible scheme similar to that used by Bentley and Leal [22] to bring the centroid closer to the stagnation point. However, there is a control method of a different kind that can be used. It is based on Poincaré–Bendixson's Theorem for possible trajectories about a saddle-point region [33]. Hence, the scheme equally requires a computer control, base on feedback provided by the video imaging of the real-time drop position.

In this work, the methodology for a wide range of studies of the dynamic of drops using **TRM** devices is presented. The deformation of drops can be studied under varied and well characterized kinematic conditions. The results of the drop dynamics here presented provide detailed experimental information under conditions that include elongation with significant amounts of vorticity.

2. Two Roll Mill geometry

A schematic of the Two-Roll Mill device is shown in Fig. 1. It consists of two cylinders of radius R with collinear axes separated by a small distance de and both rotating in the counterclockwise direction, while immersed in a fluid bath. The configuration of the flow cell used in these experiments has a fixed distance between cylinder axes de = 52.000 mm, the radii of the cylinders are R_1 = 20.518 mm and R_2 = 20.517 mm, thus with a gap, g = 10.9 mm.

The flow fields generated by a co-rotating TRM contain a stagnation point on the line between the cylinders axes, with well known local kinematic conditions characterized by its value of α. Some of the features of the flow fields generated by these mills are as follows.

(a) The flow-type parameter α (Eq. (2)), is determined only by the TRM geometry.
(b) Although these flows belong to the family of *strong flows*, simple shear flows can be approached as closely as needed by increasing the cylinder radii, thus increasing monotonically the vorticity.
(c) There exists an analytical solution that takes into account the presence of the cylinders' boundaries, in contrast with other strong flows used to study long-term effects in embedded objects, such as four-roll mills.

When using a TRM, the strength of vorticity and the shear rate can be easily varied, although with less flexibility than with a FRM [11]. Compared to Four-Roll Mills, the Two-Roll Mill requires a change of geometry for different values of α. In contrast and for a given geometry, the second invariant of the rate of deformation tensor, II_{2E}, only depends on the speed of the cylinders, and the shear rate is given by: $\dot{\gamma}_{strong}(\alpha) = \sqrt[2]{II_{2E}} = (1+\alpha)\dot{\gamma}_{shear}$.

The most important criterion for the design of TRMs is the accuracy required for the parameters of the geometry of the generated flow. For TRM geometries with equal radii, the exact solution [32] assures that the flow-type parameter at the stagnation point has a maximum value when the angular velocity is the same on each cylinder. Hence, the value of α depends only on the size of the cylinders and the separation between its axes [34,35], while the steadiness of the shear rate depends on the coupling mechanism and motor performance driving each cylinder.

For the actual geometry used in this setup, three physical length scales are critical: the exact distance between the cylinders axes, the exact diameter of cylinders, and the concentricity of all cylindrical surfaces. Assuming a machining accuracy of ±0.005 mm for all elements, the analytical solution predicts that the cell generates flows with an uncertainty of less than ±0.4% of the nominal value of α [35]. In this case, the ratio of deformation rates to vorticity, as characterized by α, is given by the half angle ϕ with the horizontal made by the incoming or outgoing flow axes at the stagnation point (see Fig. 1) in the form

$$\alpha = \tan^2(\phi). \tag{3}$$

Thus, variations of less than 0.4% in α correspond to an uncertainty of $\Delta\phi \leqslant 0.5°$. With these cylinder and gap parameters, a shear rate $\dot{\gamma} = 1\ s^{-1}$ at the stagnation point is attained with the cylinders spinning at $\omega_1 = \omega_2 = 0.2298$ rad/s.

3. Experimental device

The Two-Roll Mill experimental setup is shown in Fig. 2. It consists mainly of the Two-Roll Mill flow cell, the imaging system, the motors driving the cylinders inside de flow cell, and the real-time computer system that carries out the data processing for visualization and control of the drop (see Suppl. Material; Fig. S1). The setup is mounted on a pneumatically levitated workstation by Newport Research.

3.1. Two-Roll Mill flow cell

The TRM flow cell is made of a support for the two cylinders and an enclosure. To minimize the external wall effects on the flow field, the interior contour of the container matches a streamline (of the analytical solution) around the cylinders. It is made of black anodized aluminum to minimize internal optical reflections. The main body has an exterior cooling loop around the vertical walls

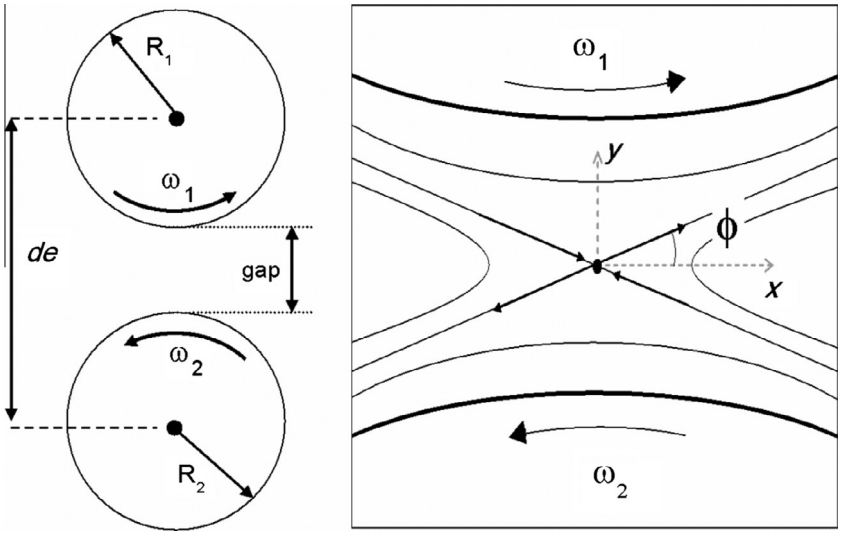

Fig. 1. (a) The Two Roll Mill device consist in two co-rotating cylinders of equal radius, with collinear axes separated by a small distance de = 52 mm, R_1 = 20.518 mm, R_2 = 20.517 mm, gap = 10.9 mm, $\omega_1 = \omega_2$ = 0.2298 rad/s for a shear rate of $\dot{\gamma} = 1\ s^{-1}$, (b) streamlines for a flow field generated by a Two Roll Mill device. The stagnation point is located on the straight line between the cylinders' axes where the incoming and outgoing axes intersect. The angle ϕ defines the flow type parameter Eq. (3).

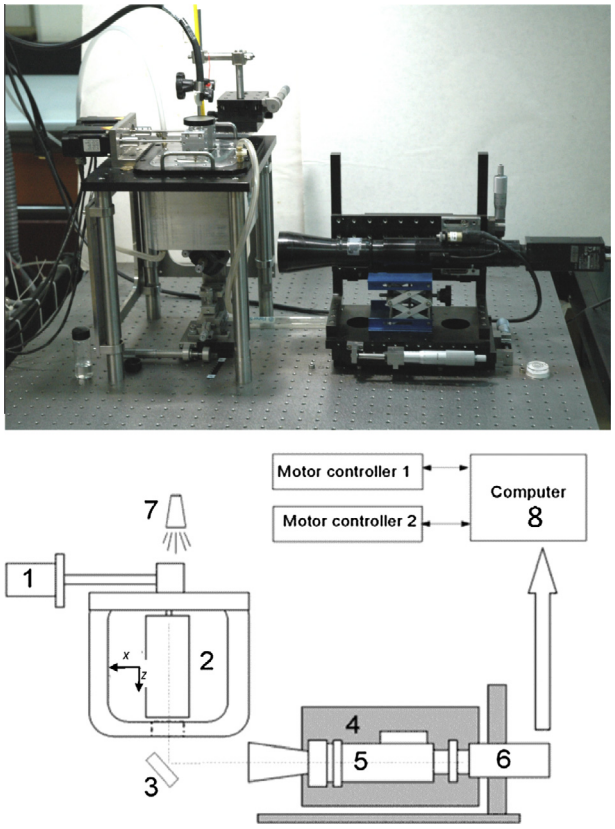

Fig. 2. Photo of the experimental setup and principal components: (1) high resolution servomotor driving each cylinder independently, (2) flow cell container, (3) mirror, (4) 3-axes displacement mount for optical system, (5) motorized zoom and focus lens, (6) CCD camera, (7) fiber optic light source, and (8) computer operating in real-time processes images and sets the motors speeds.

of the container. The cell has three optical quality windows, two on the side and one at the bottom. It is covered with a strong stainless steel lid where the cylinder supports—the housing for the worm-gear mechanism and bearing—are fastened. The lid has a large detachable acrylic window to facilitate the illumination from the top.

Each cylinder is held in position by a set of three bearings, with worm-gear and bearing preloaded for tighter operation on the radial and axial directions. The cylinders are made of two pieces, an internal shaft of small diameter made of stainless steel, (which is in contact with all bearings, bolts and gears) and the outer shell—larger in diameter—made of black-anodized aluminum. The shafts were attached permanently—by previously cryo-shrinking the shafts—inside hollowed aluminum cylinders, and subsequently machining the ensemble to the exact required external dimensions. This low-mass design reduces the rotational inertia of the cylinder while maintaining the required rigidity. The top and bottom end of the cylinder have conical shapes, with an angle that guarantees that shear rates at the top and bottom gap are smaller than the values observed within the flow field. There is a 1 mm gap between the top and bottom of the flow cell and the conical portion of the cylinders. These gaps can be filled with air (at the top) or a higher density fluid (for the bottom) of low viscosity in order to reduce the component of the velocity gradient normal to the extensional flow field.

The parallelism of the cylinder axes is maintained by the preloaded bearings. These bearing housings were all machined with the cell rigidly set on the milling machine, which guarantee a parallelism for the cylinders axes within 5 arc-seconds. The position of the lid is pin down to the flow cell by a pair of pegs—dow-pins—to maintain a top-to-bottom alignment. The cell is mounted on a rigid base to assure the highest rigidity to shear displacement with respect to the imaging systems base.

Fig. 3 shows the channels and the connectors of the cooling loop, the top transparent cover for illumination, the housing for the gears, worms and top bearings, the lateral window housing. The flow cell is placed on a rigid base where the motors that drive the cylinders are attached. Given that the cylinder axes position is fixed for the TRM geometry, different sizes of the cylinders are needed to generate flow with different values of the flow type parameter.

3.2. The optical system

The optical systems is made up of a motorized Navitar parfocal telecentric microscope [36], with a maximum magnification of 12X, an objective lens (Navitar 1-50387), an ocular lens (Navitar 1-61390, with a magnification of 2×), and a camera (IEEE 1394 CCD, model XCD-X700 by Sony) set for an image-capture rate of

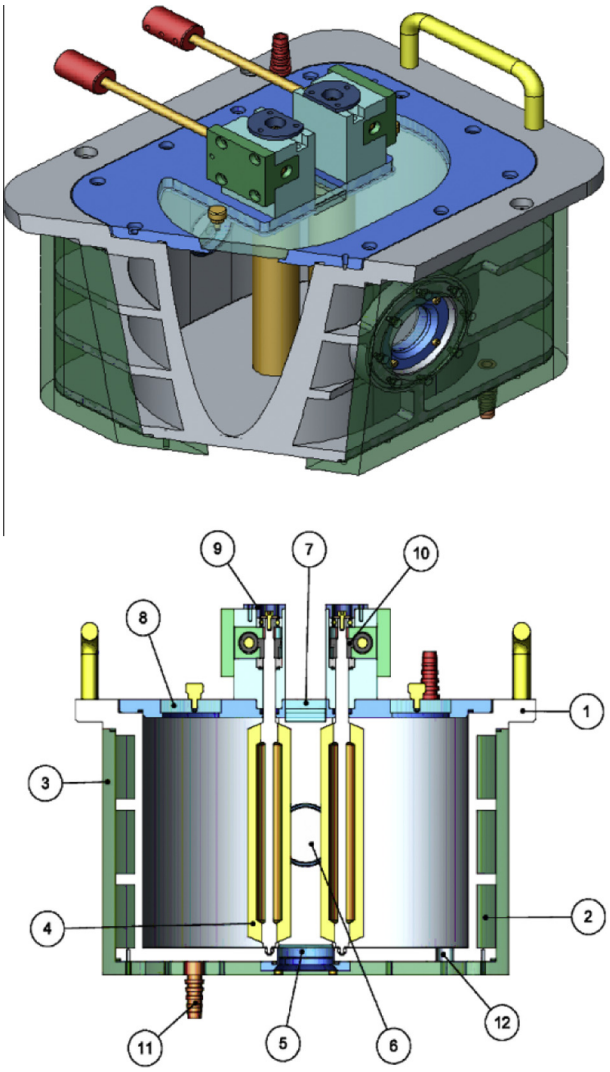

Fig. 3. Components of the flow cell TRM–B: (1) main body of the flow cell; (2) channels of the cooling loop; (3) exterior jacket of the cooling loop; (4) hollowed cylinders, with steel shaft and external black anodized cylinders; (5) bottom window assembly; (6) lateral window assembly; (7) top window assembly; (8) lid of the cell body, with top acrylic window; (9) bearings and worm-gear support of a cylinder; (10) Worm-Gear mechanism; (11) connector to the cooling loop; (12) drainage hole.

15 fps. The telecentric lens provides a constant magnification value through the depth of the field of view and image field [36]. The motorized optical system allows varying the magnification of the visual field from about 1.2 mm to 5.1 mm lengthwise (0.32× to 3.88× with the 2× Adapter) to visualize the drop size dynamics with the optimal resolution. The field of view is covered with 1024 by 768 pixels is on the x–y plane of the flow field, and is accessible through the bottom glass window using a 45 degrees mirror (with a reflective coating on the front surface) located underneath the flow cell. The optical resolution of the complete optical assembly (based on the real part of the Optical Transfer Function) is about 8 μm—or about 64 line pairs/mm, when calibrated with a 1951 USAF glass slide resolution target by Edmund Optics. The working distance at any magnification is approximately 188 mm and increases slightly as the magnification is reduced. The adjustment of the working distance required by changes in the magnification is realized by translating the optical system along the optical axis. The optical system is mounted to a base fixed to the levitated workstation, which allows precise movements in all three axes by means of precision ground slides and micrometric screws manually operated. If a better resolution is necessary, the optical train can be upgraded just by mounting higher magnification optic [36]. The bottom window protrudes into the cell about 1 mm above the bottom to have a clean view of the flow fields in the presence of the low viscosity fluids sitting at the bottom.

3.3. The data acquisition system

The data acquisition system consists of a computer Workstation HP XW4300 with a PCI SERCOS expansion card for the motors, and a Firewire interface for the imaging system. The SERCOS communicates via fiber optics with the controllers of the motors, and permits addressing the motion controllers independently. Each cylinder is driven by a servomotor coupled with a precision and preloaded worm-gear mechanism. The Kollmorgen motors AKM-11B have a rating of 125 W—with very small inertia—and are driven by Controller SERCOS Servostar 300. Communication by the motion controllers to the computer is through the dedicated PCI interface card (see Fig. S2). The steadiness to establish a given shear rate is better than 0.2% and depends primarily on the precision of the motors systems to generate the corresponding velocity of rotation.

4. Control

The implemented control is based on the Poincaré–Bendixson theorem (P–B control) for two-dimensional ordinary differential equations [33]. Reyes et al. [37] studied numerically the problem of control coupled to the solution of Stokes equations of the free surface of a drop in a container, subjected to the appropriate boundary conditions on the cylinders. These results validate a large class of experiments able to deform the drop under nominal flow conditions, while attaining long residence times near the stagnation point. This algorithm is conceptually different from the one used for the proportional control of previous studies in FRMs, which modifies the unstable nature of the saddle point by projecting continuously the drop motion along the stable direction.

In contrast, the P–B control, monitors the unstable drift of the drop, and alternates the unstable–stable directions of the flow about the drop whenever it exits the tolerance domain. This succession by turns redirects the drop centroid towards the nominal stagnation point, eventually generating a close trajectory about the saddle point, with a minimal impact upon the ideal liquid-drop dynamics (less than 5% variation, with respect to the nominal shape parameters). That is, the Poincaré–Bendixson algorithm implementation keeps the values of $\|\boldsymbol{E}\|$, and $\|\bar{\boldsymbol{w}}\|$ within a small range, hence not altering significantly the deformation rate applied upon the drop and its deformation dynamics being essentially undisturbed, thus the perturbation having a weak influence on the evolution of the drop form. Furthermore, the imposed (non-nominal) flow occurs during a brief time-lapse that is shorter than the high frequency events of the evolution of the drop deformation under study.

Execution of the experiment requires placing a drop near the central plane of the cell and about the stagnation point of the TRM flow field. Test drops are prepared using a small capillary filled with the drop's fluid and pumped inside a flask filled with the fluid of the flow cell, and subsequently transferred with a syringe to the cell, near the stagnation point. It is quite simple to prepare drops of about 50–500 μm. Using the GUI interface—described in detail in the Supplementary Material—under the manual control option, the drop is dragged towards the central region so that its centroid is inside the tolerance area.

The application of the method is simple. As the drop evolves under flow conditions, its centroid position is monitored. When the drop drifts away along the outgoing streamline and its centroid overtakes the prescribed (tolerance) domain about the nominal stagnation point, the flow is corrected by adjusting asymmetrically the nominal angular velocity of the cylinders ω_{nom}. By accelerating one cylinder to ω^{+} and decelerating the other one to ω^{-}, the position of the stagnation point is displaced toward the slower cylinder. Essentially, after the appropriate adjustment, the outgoing streamlines become incoming ones, hence reversing the direction of motion of the drop that is now towards the nominal stagnation point along a stable direction. The process is repeated as needed and the drop is confined for long times under steady and known deformation conditions (see Fig. S3).

Fig. 4 shows the streamlines of flows generated under the P–B scheme. The outer rectangle corresponds to the camera visual field and the inner shadowed rectangle represents the tolerance region where the position of the centroid of the drop is allowed to stay at the nominal flow conditions. Assume the centroid initially at Position 1, Fig. 4a. At this instant, the flow corresponds to the nominal conditions. The centroid drifts away the tolerance region until Position 2. In this instant, the control displaces the stagnation point towards the top, Fig. 4b. As a result, the stream-lines about the drop are incoming ones. Subsequently, the drop centroid is advected from Position 2 to 3; here, the flow is now reset to the nominal conditions, Fig. 4c, and the stagnation point location returns to its nominal position. The drop centroid follows the stable streamlines to reach Position 4 inside tolerance region. At Position 4, the previous process is reinitialized, but on this occasion about the lower half of the tolerance domain; so the stagnation point is relocated below the tolerance region.

4.1. Control scheme implementation

The typically observed response time for the computer interface, motor power electronics and cylinders inertia is less than 0.01 s, for changes of rotational speeds less than 5% of the preset values. The flow parameters and the position of the stagnation point are adjusted simultaneously by varying the angular velocities of both cylinders ω_1 and ω_2, keeping the shear rate $\dot{\gamma}$ constant.

4.1.1. Image acquisition

The images provided by the CCD camera are handled using the Instrumental and Industrial Digital Camera Application Programming Interface (IIDCAPI) written in the C++ language, and provided

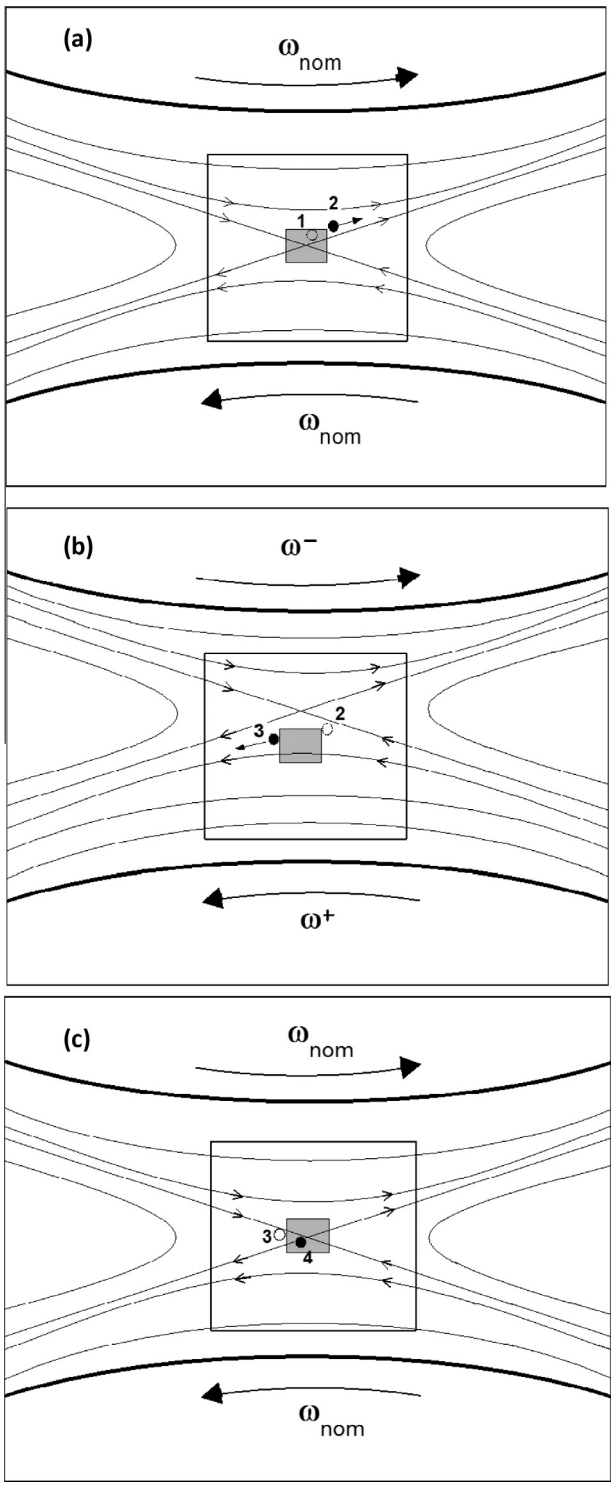

Fig. 4. Streamlines generated by a co-rotating Two-Roll Mill, showing the stagnation point in the gap between the rollers. The position of the stagnation point along the vertical can be moved changing the angular velocities of the rollers. The sequence of dots (white and black), form (a) to (c) corresponds to the starting position of the drop (unfilled circle) and final position (filled) prior to the adjustment of the position of the stagnation point by the control scheme.

by Sony. The image acquisition consists of two simultaneous processes, taking the photo and storing it in a file, and the other one is creating a temporary archive of images. The archive is a short FIFO list with a fixed number of elements and with the last image acquired by the camera available for analysis as well as a few previous ones in case of delays in processing data.

4.1.2. Image analysis

The image analysis evaluates the instantaneous position of the drop in real-time, which is the input variable for the control scheme. Using the Open Source Computer Vision Library (OpenCV) to process the raw images, the drop contour is identified applying a simple standard gray level-threshold algorithm that generates a drop image without shades of gray. This leads to a binary (black & white) image containing only the drop. For each binary image, the contour of the drop is found using the Canny algorithm, a function available in the OpenCV libraries, and then the center of mass is computed using the corresponding discrete integral. Also, in this section of the code, the ID number of the image, the coordinates of the center of mass and the size of the tolerance area of the image being processed are saved in a file. The analysis is carried out in about 1/100 of a second, regardless of the drop size, and the resolution for the position of the drop centroid is a fraction of a pixel for the smallest drops studied.

4.1.3. Adjustment of the velocities of the motors

Once the position of the center of mass is known, the algorithm evaluates next whether the center of the drop is inside the tolerance area. If it is not, the program executes de P–B control algorithm, modifying the rotation of the cylinders—assuring that an incoming flow prevails upon the drop—otherwise, the algorithm carries on under nominal flow field conditions. For details on the control strategy applied in the TRM flow cell, see references [35,37–39].

5. Calibration of the experimental flow field

The control strategy lays on two fundamental criteria: knowledge of the location of the *nominal stagnation point*—the reference location (origin) for displacements of the drop centroid—and the pattern of the streamlines (i.e., the actual value of α), which are used to predict the drop trajectory and ensure that the drop goes back to the nominal stagnation point. At the beginning of a series of experiments, the control program assumes that the center of the image—which is a few millimeters wide—is the default nominal stagnation point, with the default tolerance area being of the order of 100 μm—and centered on the image.

However, any mismatch between the actual flow field and the one taken as "default" will cause the control to fail: the real streamlines will never be predicted by the program, with the actual streamlines unable to redirect the drop towards the desired central region. Thus, the tolerance area is divided in four regions, and the P–B control takes action according the each region, with the purpose of evaluating the position of the drop inside a specific region where the streamlines are not only incoming but also ensure that the drop will remain in a stable trajectory. Those four regions are perfectly separated by the incoming and outgoing axes, whose angle, ϕ, is determined by the flow-type parameter α, described by Eq. (3).

For a given pair of cylinders inside the flow cell, the calibration routine attempts to find the exact position of the stagnation point, and to determine experimentally the precise value of α. Obtaining this information does not require visualization of all streamlines, nor the velocity fields, but knowing only the orientation of the incoming and outgoing streamlines suffices. While knowing the velocity field about the stagnation point—e.g., using PIV techniques—is possible, the fact that near the stagnation point the velocities tend to zero, makes and alternative desirable. Knowledge of the outflow and inflow streamlines is most accurate near the stagnation point, and there the analytical solution relates the flow properties uniquely with their geometrical configuration [32,35,38,39]. That is, the intersection of the streamlines provides

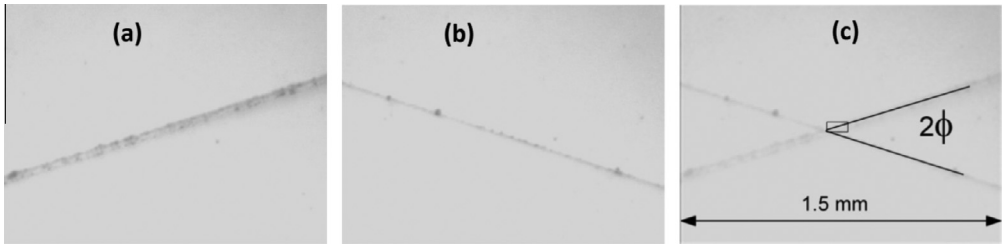

Fig. 5. Micron-size bubbles showing the outgoing axes (unstable direction of the flow) for two directions of rotation: (a) clockwise and (b) counterclockwise. (c) Overlapped photos showing the stagnation point location and the evaluation of the angle ϕ.

the exact position of the stagnation point and the angle between them the experimental value of the flow-type parameter.

To locate the streamlines, a large number of very small air bubbles is placed within the region about the stagnation point (less than 25 μm—injected in the same manner as placing the drop), with the sole purpose of being flow-tracer particles. The high viscosity of the silicon fluid and the small size of the bubbles allow using them as tracers for a sufficiently long period. With the bubbles in place, the cylinders are rotated slowly with the same angular velocity. The bubbles drift away from the central region following the outgoing streamlines. Eventually; bubbles remain only on the outgoing axis, as shown in Fig. 5a. Then the cylinders are spun in the opposite direction converting the outgoing axis into the incoming one. Now the bubbles drift back towards the central region and after a short time, as before, these drift away making it possible to visualize the line corresponding to the outgoing axis: Fig. 5b. The overlap of these two pictures allows the determination of the angle of orientation, ϕ—an experimental value for the flow-type parameter—and the actual position of the stagnation point: Fig. 5c. The experimental α value for the geometry used is $\alpha = 0.13$, corresponding to an angle of $40° \pm 0.5°$ between the outgoing and incoming axes: $\phi \cong 20°$.

The rectangle shown in this figure illustrates the tolerance area with a size of 0.1 mm × 0.05 mm. Afterwards, the optical setup main axis can be relocated to a position where the center of the image and the center of the flow field coincide. This provides the experimental procedure required for the validation of the generated flow.

6. Materials, experiments and results

The suspending fluid is a PolyDiMethylSiloxane (from Gelest Inc, DMS T35) with a measured viscosity of 5.1 Pa s and relative density of 0.973 at 25 °C. To have a clear field of view inside the cell, the suspending fluid is filtered through a 3 μm pore size paper. For the case of low viscosities ratios, the drop fluid is a vegetable canola oil, with a measured viscosity of 59 mPa s and a relative density of 0.917 at 25 °C. The ratio of viscosities is $\lambda = 0.012$ and the interfacial tension is found to be 2.7 mN/m. For the case with a high viscosity ratio, the drop fluid consisted in Poly-Isobutylene (from Polysciences Inc.) with a measured viscosity of 80 Pa s at 25 °C. For this second system the viscosity ratio is $\lambda = 15.7$ and the corresponding interfacial tension is 3.5 mN/m. All three liquids have well defined Newtonian behavior at the interval of shear rate values used. All experiments were performed at $25° \pm 0.1$ °C. We measured the viscosities of the fluids using a Rheometer Ares Model 2KFRTN1 of controlled strain, and the densities using a 10 ml pycnometer in a temperature controlled bath and an analytical balance with 0.1 mg resolution. The interfacial tension measurement method is presented in Section 7.

The drop shape is characterized mainly by two parameters: the Taylor Deformation Parameter D_T, and the orientation angle θ of the drop with respect to the flow field [13]. For small drops, one can assume an ellipsoidal cross-section shape—projected on the x-y plane of the flow—and defined in terms of L and B, the longest and shortest semi-axes, respectively. Hence, Taylor parameter is

$$D_T = \frac{L - B}{L + B}. \tag{4}$$

Using the stored drop images, measurements of the deformation parameters are made with basically the same procedure used during the control part. L and B are calculated as the two axes of the equivalent ellipse that has the same area and the same first and second moments of area as the observed drop cross section. The angle between the longest axis L and the x-axis of reference is θ. The coordinates of the center of mass, the values of the mayor and minor axes, L and B, and the orientation angle θ are stored in the file for every frame.

For simple shear flows, the confinement ratio is defined as the ratio of the drop diameter $2r_0$, to the spacing g separating the walls of the flow boundaries. The same definition $2r_0/g$ is used in this work but taking g as the gap for the TRM geometry (the distance between cylinders surfaces, Section 3.1). Accordingly, the degree of confinement seems to have an appreciable effect on drop dynamics only when $2r_0/g > 0.3$ [40]. For all experiments here reported, the radii of the drops were in the range $0.4 < r_0 < 0.7$ mm, so the degree of confinement is lower than 0.13, and observed phenomena is essentially that of a drop free of boundary effects.

The deformation histories for the drop shape presented subsequently correspond to the observed dynamics after start-up of steady shear deformation as well as the dynamics after a steady shear flow is suddenly stopped and the drop form relaxes to the spherical shape is presented.

6.1. Drops with low viscosity ratio

The behavior for drop deformation and breakup—for the limiting cases of simple shear and elongational flow—was previously reported [13,16,23,41,42]. With the TRM and for all low viscosity drops, when the relative flow stresses are weak with respect to the capillary force—i.e. the capillary number Ca of the imposed flow is lower than the critical value [16]—the drop deforms as well into a prolate spheroid with $\theta \cong 45°$. This orientation is also observed for simple shear flows as well as flow generated with TRMs and FRMs. In contrast, with increasing Ca, D_T augments, while θ rotates towards the outflow axis defined by ϕ—values that are not possible with PBs nor FRMs. Fig. 6 shows the typical transient drop deformation and orientation curves of the response of the drop to the start-up a strong flow with vorticity, under weak capillary numbers. The evolution of D_T and θ are plotted as a function of the time, for different values of Ca until the deformation and orientation reached a steady state value.

But, once Ca is larger than a critical value, Ca_{crit}, the drop does not reach an equilibrium shape but continues deforming at a fairly

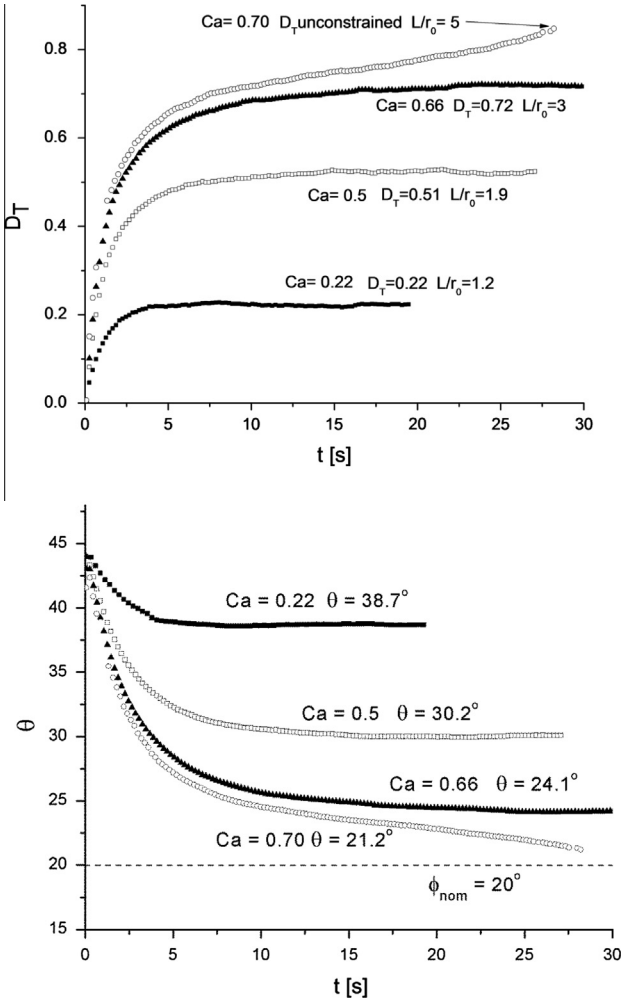

Fig. 6. Taylor's deformation, elongation parameter L/r_0 of the drop (a), and orientation curves (b) for $\alpha = 0.13$ and $\lambda = 0.012$ and different capillary numbers. The orientation angle of the TRM corresponding to $\alpha = 0.13$ is $\phi_{nom} = 20°$.

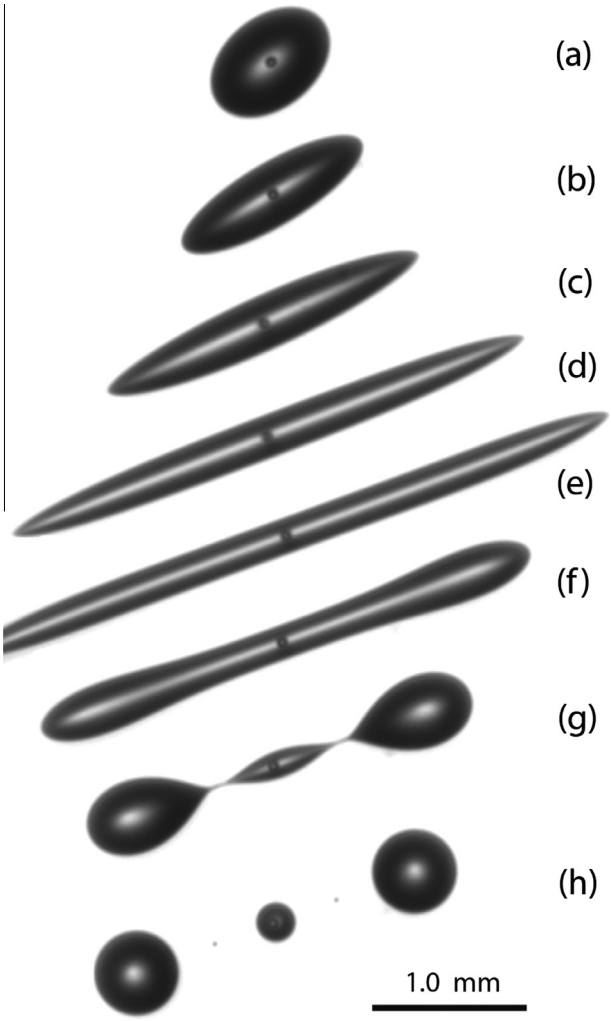

Fig. 7. Drop deformation and orientation for a drop with $r_0 = 0.35$ mm, for different values of the capillary numbers for $\alpha = 0.13$ and $\lambda = 0.012$. The corresponding parameters of the images are listed in Table 1.

constant rate and its orientation angle θ approaches that corresponding to the characteristic of the flow-type: $\phi = 20°$ (see Fig. 6). However, the experimentally determined critical capillary number $Ca_{crit} = 0.70 \pm 0.01$—for $\alpha = 0.13$ and $\lambda = 0.012$, see Fig. S4—is significantly larger than that corresponding to $\alpha = 0.2$—with a $Ca_{crit} \cong 0.47$ [23]—but lower than that corresponding to $\alpha = 0$, which is found to be about 1 [16].

If the flow persists for $Ca > Ca_{crit}$, the drop eventually breaks up. Beyond a certain degree of deformation, the drop becomes clearly rod-shaped and the parameter D_T is a less sensitive measure of deformation; see Fig. 7. Thus, for elongated drops it is convenient to characterize their shapes using the dimensionless elongation parameter L/r_0 as the appropriate parameter. Fig. 7(a)–(c) shows the steady state drop shape and orientation reached for $Ca < Ca_{crit}$, and Fig. 7(d), and (e) show the evolution of those parameters when $Ca > Ca_{crit}$. In latter Figures, it can be seen how the drop continues elongating as long as the flow is maintained and the drop is aligned with the outgoing axis; i.e., $\theta \cong \phi$. Fig. 7(f)–(h) correspond to the waist-pinching breakup process that occurs for a rod-shaped drop, after the flow has been stopped. Table 1 present the values for Ca, D_T, θ, and L/r_0 for the evolution of the deformation under steady flow conditions, just before the maximum deformation is achieved—shown in Fig. 7.

Figs. 8 and 9 show major differences between the steady state deformation and orientation of the drop, of the observed experimental data for $\alpha = 0.20$ [23] and $\alpha = 0.13$, as a function of Ca. There appears to be a closer correlation between the experimental data for $\alpha = 0.13$ and the Taylor theory for simple shear flow, with a clear departure for more "elongational" type of flows. Also, it appears that the theoretical model of Taylor for simple shear flow, based on small deformation theory, is valid for a wider range of deformation values for the former flow that the latter cases. Thus, it would indicate that, for flows close to that of simple shear flow, small differences in the value of the flow-type parameter can strongly affect the drop behavior. Besides, the maximum deformation for $\alpha = 0.13$ and 0.2 appears to be approximately the same: $D_{T,\,max} = 0.72$, and may indicate that the dominant interfacial tension becomes unstable.

6.2. Drops high viscosity ratio

For viscous drops, with $\lambda \gg 1$ and under stresses due to a TRM flow, its deformation behavior is different from those with $\lambda < 1$. In the former case, the interfacial stresses have a quasi-homogeneous value over the complete surface of the drop; the maximum deformation is a fraction of that observed low viscosity drops, with a drastic departure from surface stress values present on a very elongated low viscosity drop. Thus, the interfacial tension has a weak effect in the flow and on the drop shape, with the flow vorticity

Table 1
Parameters corresponding to the drop states in Figs. 6 and 7.

	(a)	(b)	(c)	(d) t = 28 seg.	(e) Flow stopped at t = 30 seg
Ca	0.22	0.5	0.66	0.70 Breakup condition	0.70
D_T	0.22	0.51	0.72	8.7	–
θ	38.7°	30.2°	24.1°	21.1°	20.5°
L/r_0	1.2	1.9	3	5	6.4

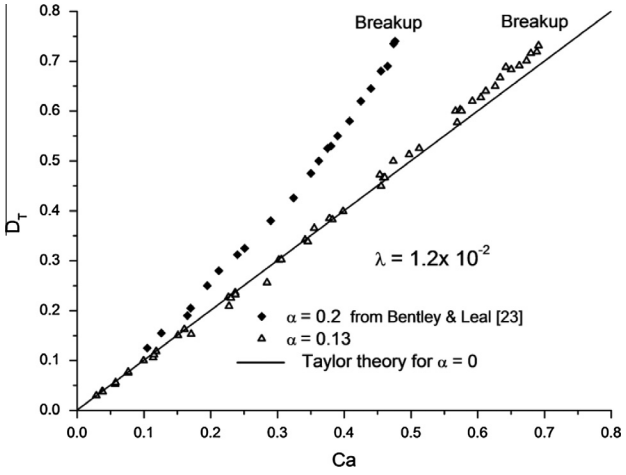

Fig. 8. Steady state deformation for $\lambda = 0.012$ and (a) $\alpha = 0.13$, and (b) $\alpha = 0.2$ (filled symbols correspond to Bentley and Leal [23]). The continuous lines correspond to Taylor's theory for $\alpha = 0$—simple shear flow.

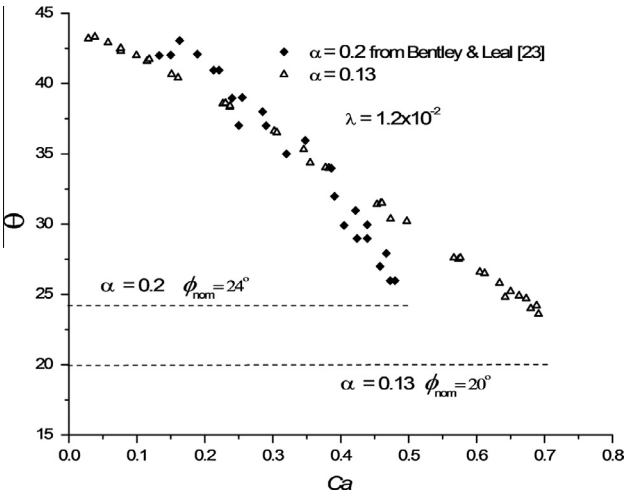

Fig. 9. Steady state orientation for $\lambda = 0.012$ and (a) $\alpha = 0.13$, and (b) $\alpha = 0.2$ (filled symbols correspond to Bentley and Leal [23]).

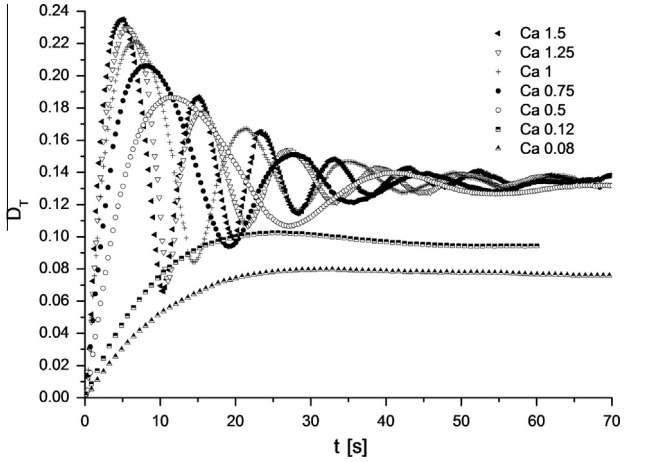

Fig. 10. (a) Time-dependent Taylor's deformation traces for high capillary numbers, corresponding to $\alpha = 0.13$ with $\lambda = 16$. Overshoots present for $Ca > 0.12$.

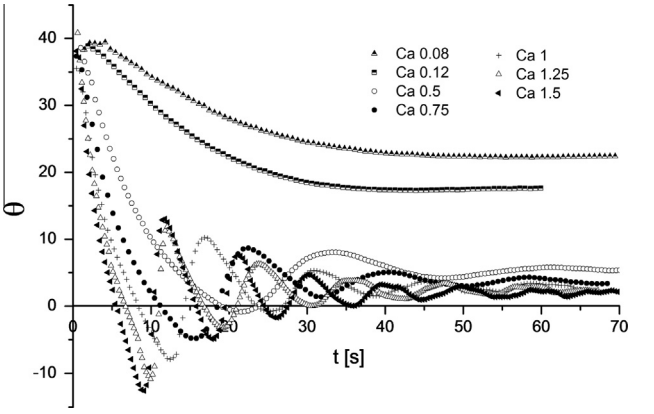

Fig. 11. Time-dependent orientation curves for low and high value of the Capillary numbers corresponding to $\alpha = 0.13$ with $\lambda = 16$.

playing a dominant role; hence, the maximum deformation observed depends mainly on the viscosities ratio and the flow-type parameter. For low values of capillary number, say $Ca < 0.12$ (see Figs. 10 and 11), the transient deformation and orientation curves show a behavior similar to that for low viscosities ratio where the steady-state deformation and orientation are reached monotonically and depend linearly on the capillary number; steady shapes are essentially spherical under these conditions.

As Ca increases, $Ca > 0.12$, the transient deformation and orientation curves present overshoots and undershoots respectively; see Fig. S5. For larger capillary numbers, $Ca > 0.5$, steady states are reached only after a transient oscillatory behavior, similar to the analytical predictions by Cox [43] and observed experimentally by Torza et al. [15] for simple shear flow (see Figs. 10 and 11). This behavior has also been observed for steady flow dynamics of polymer solutions under elongational flows with small α values [30], but not with previous drop experiments. In Figs. 10 and 11, the deformation curves for large Ca show a damped oscillations with frequency and maximum amplitude depending on Ca, and the relaxation time can be approximated by $\tau \simeq \lambda Ca/\dot{\gamma}$.

For $Ca \geqslant 0.5$, Fig. 10 shows the steady state deformation attaining its maximum value, which depends on the viscosities ratio and the type of flow. The orientation curves, shown in Fig. 11, indicate that a steady state is reached after a short-live period, after the drop spins about its centroid several times, and settles aligned

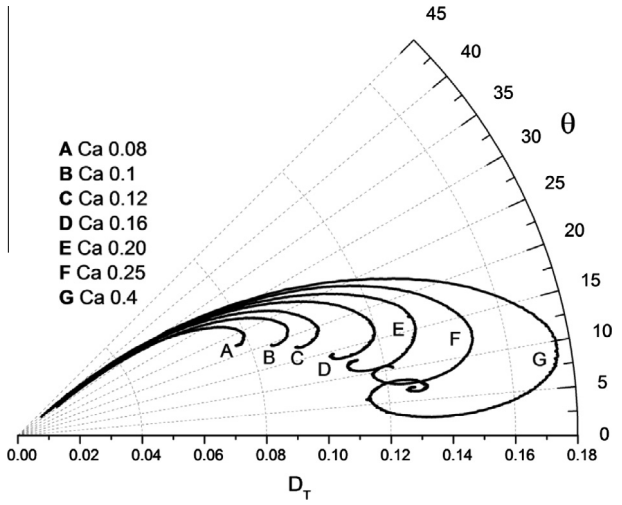

Fig. 12. Polar plot of the evolution of D_T and θ parameters for low values of capillary numbers corresponding to $\alpha = 0.13$ with $\lambda = 16$.

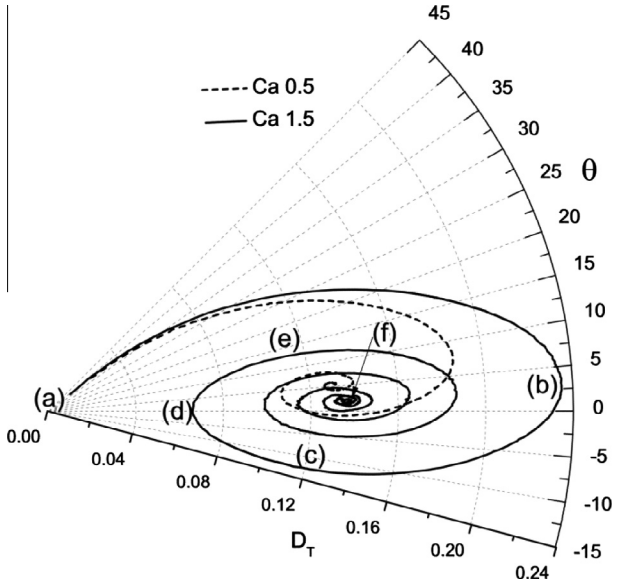

Fig. 13. Polar plot of the evolution of D_T and θ parameters for high values of capillary numbers corresponding to $\alpha = 0.13$ with $\lambda = 16$. At instant points (a) to (e) the values of the shape parameters are listed in Table 2. Fig. S5 shows the drop images for the same instant points (a) to (e).

close to the *x*-axis. That is, the steady orientation angle can attain values below the outflow axis (see Fig. S6), with the magnitude of the deformation rate having a weak contribution, and the vorticity playing a more dominant role. Furthermore, during the transient evolution, the orientation angle may attain repetitively negative values for an ellipsoidal shape with respect to the *x*-axis of the flow—very close to stable axis—before settling at a positive value

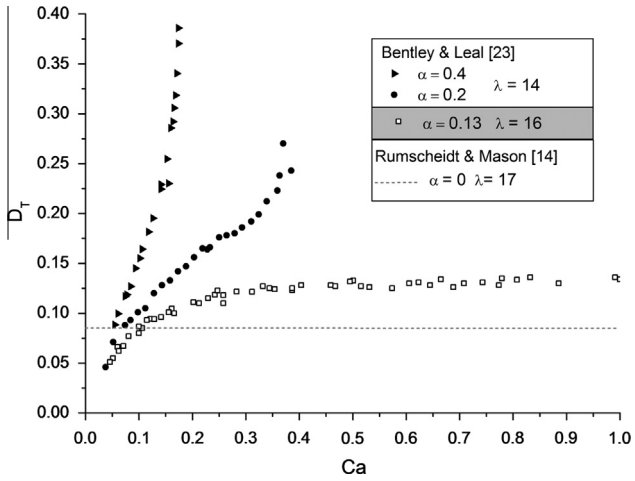

Fig. 14. Steady state deformation as function of the capillary number for different values of the type of flow parameter and high viscosity ratios.

just larger than zero; see Fig S7. Hence, the instantaneous deformation rate actively reduces its attained elongation.

Figs. 12 and 13 are polar plots of the evolution of D_T and θ parameters for low and high values of *Ca*, respectively, in a similar way as Torza et al. [15], Cox [43], Rallison [44] and more recently with numerical simulation by Pozrikidis and coworkers [45]. All reported trajectories show the cyclical evolution of those parameters from the onset up to the final steady state. The general overview of experimental results for low *Ca* values, show the steady deformation rising up rapidly and the final orientation angle approaching zero; see Fig. 12. For larger *Ca* numbers, all traces perform multiple cycles before reaching the steady state. For high values of *Ca* (see Fig. 13), increments on *Ca* have a minimum effect on the steady states values, but a remarkable effect on the number of cycles needed for the drop to reach those stationary states. Torza et al. [15] have shown this effect for drops in simple shear flows, although with some experimental limitations. Cox, Rallison and Pozrikidis and collaborators [43–45], have replicated with analytical or numerical results this behavior for shear flows and viscosity ratios $\lambda \geqslant 25$, but no data have been reported for values of the flow-type parameter or viscosity ratios presented in this work. However, there are significant quantitative differences that will be addressed in a future report; in particular, the observed attenuation is faster that the numerical or analytical predictions.

Figs. 14 and 15 show the experimental steady states parameters D_T and θ as a function of the *Ca*, for different flow-type parameters and similar viscosities ratio. The traces show that whereas flow fields with $\alpha \geqslant 0.2$ are able to break apart the drop, a small increase in the vorticity of the flow field—for $\alpha \simeq 0.13$—makes it impossible to carry out rupture; see Fig 14. Instead, we found that the maximum steady deformation allowed by the high viscosities ratio and the flow-type parameter $\alpha = 0.13$ is $D_T = 0.13$, while for $\alpha = 0$ and the same magnitude of viscosities ratio is found to be $D_T \simeq 0.085$; See Fig. 14 and Ref. [14]. Furthermore, the orientation angle approaches cero as *Ca* increases, and seems to have a

Table 2
Parameters of the drop evolution at the instants marked by letters in Fig. 13.

	(a) Initial shape	(b) Maximum deformation	(c) Minimum angle	(d) Minimum deformation	(e) Maximum angle	(f) Steady state
t (s)	0	4.6	9	10.33	11.6	$t > 70$
D_T	0	0.23	0.11	0.066	0.10	0.13
θ	–	4.5°	−12.7°	−0.4°	13°	1°

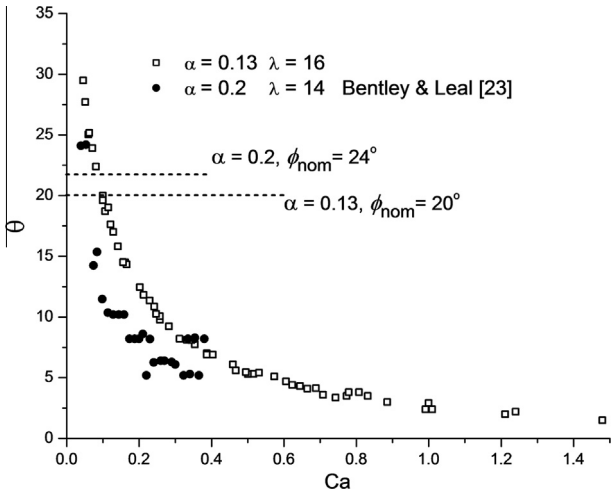

Fig. 15. Steady state orientation as function of the capillary number for different values of the type of flow parameter and high viscosity ratios.

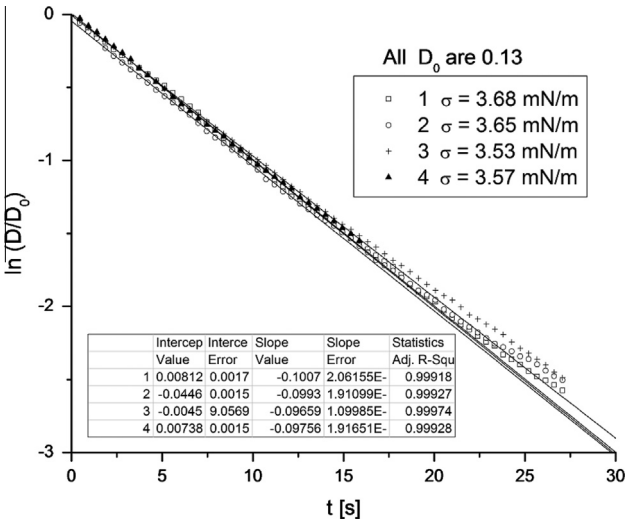

Fig. 16. Linear fit for data of the retraction process of a drop with $r_0 = 0.47$ and a viscosities ratio $\lambda = 16$. The upper text box shows the interfacial tension values calculated from the slope of each retraction process.

stronger dependence on the capillary number as shown in Fig. 15. These angle values are well below the orientation of the unstable flow direction ϕ; see Figs. S6 and S7. These results might be attainable only because of the used of the TRM flow configuration, within a space of parameters not previously studied, nor experimentally accessible.

7. Interfacial tension

The interfacial tension between fluid systems can be calculated using the deformed drop retraction method (DDR). This method is most useful when the density difference between the two liquids is very small, or inexistent, because it depends only on the dynamic properties of the fluids. The principle of DDR is to determine the interfacial tension from the measure of the dimensions of an ellipsoidal deformed drop in its evolution from an initial deformation D_0 to a final spherical shape. An equation describing the evolution of a deformed drop toward an equilibrium spherical form is obtained by Mo et al. [46] from the evolution equation proposed by Maffetone et al. [47]. In this equation, the drop shape is described by a symmetric, positive-definite, second rank tensor $\boldsymbol{S}$ whose eigenvalues Λ represent the square semi-axes of the ellipsoid that represents the deformed drop. Hence, to describe de drop relaxation the shape parameter $D = \Lambda_1 - \Lambda_2$ is used; where $\Lambda_1 = L^2 = r_{max}^2$ and $\Lambda_2 = B^2 = r_{min}^2$ [47].

$$D(t) = D_0 \exp\left(\frac{-t}{\tau}\right), \tag{5}$$

with

$$\frac{1}{\tau} = \frac{\sigma}{\mu_1 r_0}\left[\frac{40(\lambda+1)}{(2\lambda+3)(19\lambda+16)}\right]. \tag{6}$$

In the process of ellipsoidal drop retraction, λ, μ_1, σ and r_0 are constants, then σ can be calculated from the slope of $\ln(D/D_0)$versus time t.

Fig. S5 is an example of the deformation evolution for an experiment of high viscosity ratio drop. The transitory and steady states can be observed in the plots, steady-state conditions are maintained as long as the flow is applied and once the flow is stopped the drop relaxes to its spherical shape (region of retraction).

Given that the retraction process is independent from the deformation process, the data for all experiments can be used regardless of the flow type, or shear rate. In this case, it is possible to obtain a value of the interfacial tension every time the drop is deformed. Each retraction process has a characteristic curve for the exponential relaxation. If the conditions for the experiments do not change, i.e., μ_1, σ and λ are constant, it is expected to get only one common value for the interfacial tension in all of experiments. Liu, et al. [48] carried out an extensive revision for calculation of interfacial tension using DDR methods and found that the initial deformation, D_0, is very important in measuring the interfacial tension, and in order to calculate the most reliable value the optimum initial retraction shape corresponds to a deformation value of $D_0 = D_T \cong 0.15$. Fig. 16 shows plots for the time evolution of retraction for a drop and the linear fit for each one, as well as the interfacial tension values obtained for $\lambda = 16$. The interfacial tension for $\lambda = 0.012$ is calculated in the same way.

8. Conclusions

The computer-controlled Two-Roll Mill flow cell, presented in this paper allows studies of drop and particle dynamics in flow fields with values of the flow type parameter α, not accessible for any other device. Like other extensional (or elongational) flows, the drop is placed at the stagnation point where is subjected to a saddle-point stability environment. The control implemented is robust enough to retain the embedded object in the desired region for long experimental times and under the specified flow conditions. Along with the high performance components of the setup, it is possible to perform long-time and high deformation experiments of drop, with high accuracy. The results presented here show the effect of the flow field with $\alpha = 0.13$ on the dynamics of drop deformation for two extreme values of viscosities ratio, these results present a smooth transition with respect to previous data available for $\alpha = 0$ and $\alpha = 0.2$. The interfacial tension needed to characterize the flow conditions was successfully measured with high accuracy through the DDR method using the data provided by the TRM experiments, overcoming the problems that appear in other methods when high viscous fluids are used or very low difference of densities are present. The present flow cell can be used to perform numerous experiments including the study of drop deformation and breakup for a wider range of viscosities under flow fields covered by the TRM—not feasible until now—or with non-Newtonian fluids. Other possible experiments include the

dynamics of drops near walls with elongational conditions—conditions not amenable to study with earlier flow devices—and with the presence of surfactants or other polymeric additives, which are of technological relevance. Drop phenomena analyzed with this experimental setup, have similar kinematics, from the point of view of the applicable boundary conditions, as well as dynamically to the slow flow hydrodynamics of two-phase flows trough pores and fractures.

Acknowledgments

The authors gratefully acknowledge the anonymous reviewers for reading the manuscript with great care, and for their suggestions and recommendations, whose comments led to this improved version. IYR thanks UNAM-CEP for the Graduate Scholarship, EG thanks funding N. 513247Y and N. 225981 from CONACyT Basic Science Program. EG, AAM and MAHR thank funding N. IG100714 from UNAM-PAPIIT and AAM thank support from Fenomec Program.

Appendix A. Supplementary material

Supplementary data associated with this article can be found, in the online version, at http://dx.doi.org/10.1016/j.expthermflusci.2014.08.006.

References

[1] D. Megias-Alguacil, K. Feigl, M. Dressler, P. Fischer, E.J. Windhab, Droplet deformation under simple shear investigated by experiment, numerical simulation and modeling, J. Non-Newtonian Fluid Mech. 126 (2005) 153–161.
[2] N. Grizzuti, O. Bifulco, Effects of coalescence and breakup on the steady-state morphology of an immiscible polymer blend in shear flow, Rheol. Acta 36 (1997) 406–415.
[3] M. Minale et al., Effect of shear history on the morphology of immiscible polymer blends, Macromolecules 30 (18) (1997) 5470–5475.
[4] S.P. Lyu et al., Coalescence in polymer blend during shearing, AIChe 46 (2) (2000) 229–238.
[5] K.M.B. Jansen et al., Droplet breakup in concentrated emulsions, J. Rheol. 45 (1) (2001) 227–236.
[6] S.P. Lyu et al., Modeling of coalescence in polymer blends, AIChe 48 (1) (2002) 7–14.
[7] S. Caserta et al., Shear-induced coalescence in aqueous biopolymer mixtures, Chem. Eng. Sci. 60 (4) (2005) 1019–1027.
[8] S. Caserta et al., Drop deformation in sheared polymer blends, J. Rheol. 51 (4) (2007) 761–774.
[9] S. Caserta, S. Guido, Vorticity banding in biphasic polymer blends, Langmuir 28 (2012) 16254–16262.
[10] A. Pommella et al., Shear-induced deformation of surfactant multilamellar vesicles, PRL 108 (2012) 138301(4).
[11] E. Boonen et al., Single droplet break-up in controlled mixed flows, Appl. Mater. Interfaces 2 (7) (2010) 2140–2146.
[12] K. Verhulst, P. Moldenaers, Drop shape dynamics of a Newtonian drop in a non-Newtonian matrix during transient and steady shear flow, J. Rheol. 51 (2) (2007) 261–273.
[13] G.I. Taylor, The formation of emulsions in definable fields of flow, Proc. R. Soc. London, Ser. A 146 (1934) 501–523.
[14] F.D. Rumscheidt, S.G. Mason, Particle motions in sheared suspensions. XII. Deformation and burst of fluid drops in shear and hyperbolic flow, J. Colloid Sci. 16 (1961) 238–261.
[15] S. Torza, R.G. Cox, S.G. Mason, Particle motions in shear suspensions, J. Colloid Interface Sci. 38 (2) (1972) 395–411.
[16] H.P. Grace, Dispersion phenomena in high viscosity immisible fluid systems and application of static mixers as dispersion devices in such systems, Chem. Eng. Commun. 14 (1982) 255–277.
[17] S. Guido, M. Villone, Three-dimensional shape of a drop under simple shear flow, J. Rheol. 42 (1998) 395–415.
[18] S. Guido, F. Greco, M. Villone, Experimental determination of drop shape in slow steady shear flow, J. Colloid Interface Sci. 219 (1999) 298–309.
[19] S. Guido, M. Minale, P.L. Maffetone, Drop shape dynamics under shear-flow reversal, J. Rheol. 44 (2000) 1385–1399.
[20] S. Guido, F. Greco, Drop shape under slow steady shear flow and during relaxation. Experimental results and comparison with theory, Rheol. Acta 40 (2001) 176–184.
[21] Birkhoffer, H. Beat, et al., Computer-controlled flow cell for the study of particle and drop dynamics in shear flow fields, Ind. Eng. Chem. Res. 44 (2005) 6999–7009.
[22] B.J. Bentley, L.G. Leal, A computer-controlled four-roll mill for investigations of particle and drop dynamics in two-dimensional linear shear flows, J. Fluid Mech. 167 (1986) 219–240.
[23] B.J. Bentley, L.G. Leal, An experimental investigation of drop deformation and breakup in steady two-dimensional linear flows, J. Fluid Mech. 167 (1986) 241–283.
[24] H.A. Stone, B.J. Bentley, L.G. Leal, An experimental study of transient effects in the breakup of viscous drops, J. Fluids Mech. 173 (1986) 131–158.
[25] W.J. Milliken, H.A. Stone, L.G. Leal, The effect of surfactant on the transient motion of newtonian drops, Phys. Fluids 5 (1993) 69–79.
[26] G. Astarita, Objective and generally applicable criteria for flow classification, J. Non-Newtonian Fluids Mech. 6 (1979) 69–76.
[27] W.L. Olbricht, J.M. Rallison, L.G. Leal, Strong flow criteria based on microstructure deformation, J. Non-Newtonian Fluid Mech. 10 (1982) 291–318.
[28] M.S. Chong, A.E. Perry, B.J. Cantwell, A general classification of three dimensional flow fields, Phys. Fluids A 2 (1990) 765–778.
[29] H. Yang, C.C. Park, Y.T. Hu, L.G. Leal, The coalescence of two equal-sized drops in a two dimensional linear flow, Phys. Fluids 13 (5) (2001) 1087–1106.
[30] E. Geffroy, L.G. Leal, Flow birefringence of a concentrated polystyrene solution in a Two Roll-Mill 1. Steady flow and start-up of steady flow, J. Polym. Sci. B: Polym. Phys. 30 (12) (1992) 1329–1349.
[31] J.J. Wang, D. Yavich, L.G. Leal, Time resolved velocity gradient and optical anisotropy in lineal flow by photon correlation spectroscopy, Phys. Fluids 6 (11) (1994) 3519–3534.
[32] M.A.H. Reyes, E. Geffroy, A co-rotating two-roll mill for studies of two-dimensional, elongational flows with vorticity, Phys. Fluids 12 (10) (2000) 2372–2376.
[33] S. Ross, Differential Equations, Wiley & Sons, 1984.
[34] M.A.H. Reyes, E. Geffroy, Study of low Reynolds number hydrodynamics generated by symmetric co-rotating two-roll mills, Revista Mexicana de Física 46 (2) (2000) 135–147.
[35] M.A.H. Reyes, Hydrodynamics of deformable objects in creeping flows. PhD thesis. UNAM. Mexico, 2005.
[36] Navitar Optics Web page: <http://www.navitar.com/product/12x-lens-attachments.aspx> Visited on July 26, 2014:.
[37] M.A.H. Reyes, A.A. Minzoni, E. Geffroy, Numerical study of the effect of nonlinear control on the behavior of a liquid drop in elongational flow with vorticity, J. Eng. Math. 71 (2) (2011) 185–203.
[38] Israel Y. Rosas, Marco A.H. Reyes, A.A. Minzoni, E. Geffroy, Nonlinear control applied to the rheology of drops in elongational flows with vorticity, in: Meral Altinay (Ed.), Applications of Nonlinear Control, InTech, Croatia, 2012, pp. 37–56.
[39] Israel Y. Rosas, Experimental study of the deformation of a drop immersed in a elongational flow with vorticity. PhD thesis. UNAM. Mexico, 2013.
[40] P. Van Puyvelde et al., Review on morphology development of immiscible blends in confined shear flow, Polymer 49 (2008) 5363–5372.
[41] H.A. Stone, L.G. Leal, Relaxation and breakup of an initially extended drop in an otherwise quiescent fluid, J. Fluid Mech. 198 (1989) 399–427.
[42] H.A. Stone, Dynamics of drop deformation and breakup in viscous fluids, Ann. Rev. Fluid Mech. 26 (1994) 65–102.
[43] R.G. Cox, The deformation of a drop in a general time-dependent fluid flow, J. Fluid Mech. 37 (1969) 601–623.
[44] J.M. Rallison, The deformation of small viscous drops and bubbles in shear flows, J. Fluid Mech. 16 (1984) 45–66.
[45] M.R. Kennedy, C. Pozrikidis, R. Skalak, Motion and deformation of liquids drops and the rheology of dilute emulsions in simple shear flow, Comput. Fluids 23 (2) (1994) 251–278.
[46] H. Mo et al., A new method to determine interfacial tension from the retraction of ellipsoidal drops, J. Non-Newtonian Fluid Mech. 91 (2000) 221–232.
[47] P.L. Maffettone, M. Minale, Equation of change for ellipsoidal drops in viscous flow, J. Non-Newtonian Fluid Mech. 78 (1998) 227–241.
[48] Y. Liu et al., Studies on some factors influencing the interfacial tension measurement of polymers, Polymer 46 (2005) 2811–2816.